

## Neutrophil Transit Times through Pulmonary Capillaries: The Effects of Capillary Geometry and fMLP-Stimulation

Mark Bathe,\* Atsushi Shirai,\* Claire M. Doerschuk,<sup>†</sup> and Roger D. Kamm\*

\*Department of Mechanical Engineering and Division of Biological Engineering, Massachusetts Institute of Technology Cambridge, Massachusetts 02139 and <sup>†</sup>Department of Pediatrics, Rainbow Babies and Children's Hospital and Case Western Reserve University, Cleveland, Ohio 44106 USA

**ABSTRACT** The deformations of neutrophils as they pass through the pulmonary microcirculation affect their transit time, their tendency to contact and interact with the endothelial surface, and potentially their degree of activation. Here we model the cell as a viscoelastic Maxwell material bounded by constant surface tension and simulate indentation experiments to quantify the effects of (*N*-formyl-L-methionyl-L-leucyl-L-phenylalanine (fMLP)-stimulation on its mechanical properties (elastic shear modulus and viscosity). We then simulate neutrophil transit through individual pulmonary capillary segments to determine the relative effects of capillary geometry and fMLP-stimulation on transit time. Indentation results indicate that neutrophil viscosity and shear modulus increase by factors of 3.4, for  $10^{-9}$  M fMLP, and 7.3, for  $10^{-6}$  M fMLP, over nonstimulated cell values, determined to be 30.8 Pa·s and 185 Pa, respectively. Capillary flow results indicate that capillary entrance radius of curvature has a significant effect on cell transit time, in addition to minimum capillary radius and neutrophil stimulation level. The relative effects of capillary geometry and fMLP on neutrophil transit time are presented as a simple dimensionless expression and their physiological significance is discussed.

### INTRODUCTION

Neutrophils are larger in average diameter than about 40% of capillary segments in the human lungs (Doerschuk et al., 1993), and transit between 50 and 100 segments in a single pass through the extensively interconnected pulmonary microcirculation (Hogg et al., 1994). These factors, together with their decreased deformability relative to erythrocytes, cause neutrophils to be delayed for seconds or even longer before they deform sufficiently to transit individual pulmonary capillary segments, and result in an increased concentration of the cells in the pulmonary capillary blood with respect to erythrocytes (Lien et al., 1987, 1990, 1991; Doerschuk, et al., 1993, 2001; Hogg et al., 1994). Chemoattractants such as *N*-formyl-L-methionyl-L-leucyl-L-phenylalanine (fMLP), which have been shown to decrease neutrophil deformability, also increase neutrophil concentration in the lungs (Worthen et al., 1989; Lipowsky et al., 1991).

We recently used a computational network model of the pulmonary microcirculation to estimate pressure drops in the lung. Normal segmental pressure drops were found to be  $\sim 10$  Pa (0.1 cmH<sub>2</sub>O), increasing locally by 100–300% when a local capillary segment was blocked by a deforming neutrophil (Huang et al., 2001). In that study, the transit time of a neutrophil through an individual capillary segment was based in part on results of micropipette aspiration experiments (Fenton et al., 1985) and in part on theoretical predictions of cell entrance into a micropipette (Yeung and Evans, 1989) (neutrophil “entrance time” and “transit time”

are considered synonymous in this study because we are only concerned with transit through capillaries that are relatively short and narrow, so that the bulk of the cell's transit time consists of its entering into the narrowest part of the capillary segment). Though the expression incorporated the separate effects of driving pressure and minimum capillary radius on neutrophil transit time, it was based on studies using blunt-ended micropipettes. We noted, however, that capillary geometry could significantly influence neutrophil transit times and that entrance curvature and lack of axisymmetry were important effects to consider. This provided the primary motivation for the present study, namely to obtain a more general expression for neutrophil transit time that addresses the effects of entrance geometry. We also sought to better understand the relative importance of cell activation level on transit time through the pulmonary capillaries.

To address these issues, an existing neutrophil model was selected from the literature and appropriate model parameter values were determined for its nonstimulated behavior and for two levels of stimulation produced by treatment with fMLP ( $10^{-9}$  and  $10^{-6}$  M). We modeled the cell as a homogeneous viscoelastic Maxwell material with a constant bounding surface tension of 31 pN/ $\mu$ m (Dong et al., 1988). The Maxwell model parameter values (elastic shear modulus  $G_{\text{cell}}$  and viscosity  $\mu_{\text{cell}}$ ) were determined by simulating previously performed indentation experiments (Worthen et al., 1989) on nonstimulated and fMLP-stimulated neutrophils, and varying the parameters to best fit the experimental data. In the subsequent phase of the study, we modeled and simulated neutrophil transit through individual, axisymmetric pulmonary capillary segments. Minimum capillary radius and capillary entrance geometry (more specifically, the radius of curvature of the constriction) were varied to quan-

Submitted September 18, 2001, and accepted for publication May 29, 2002.

Address reprint requests to Roger D. Kamm, 3-260, 77 Massachusetts Ave., Cambridge, MA 02139. Tel.: 617-253-5330; Fax: 617-258-8559; E-mail: rdkamm@mit.edu.

© 2002 by the Biophysical Society

0006-3495/02/10/1917/17 \$2.00

tify their respective effects on transit time. For this purpose, we performed a fully coupled fluid–solid interaction finite element analysis using a nonlinear kinematic description for the cell and an arbitrary Lagrangian–Eulerian (ALE) formulation for the surrounding plasma. Effects of cell–capillary wall adhesion and time-varying cellular behavior during transit, such as actin polymerization, were neglected.

In what follows, we begin by presenting the continuum mathematical models used for nonstimulated and fMLP-stimulated neutrophils (they are geometrically and constitutively identical, differing only in the specific values of their constitutive constants determined from the indentation experiments), the indentation experiment, and pulmonary capillary segments. We then present the essential features of the finite element methods used to obtain their solutions. Indentation results are presented next, followed by our predictions of dimensionless capillary transit times. A simple, closed-form expression that fits the data in the Newtonian, or viscous deformation-dominated, limit is presented, as well as a correction that accounts for the effects of cellular elasticity. Dimensionless and dimensional transit times are considered in a physiological context in the Discussion that follows, in which the relative effects of fMLP and capillary geometry on cell transit time are addressed.

## MODELING

### The neutrophil

Of the various mechanical models that have been proposed for the neutrophil, three are most widely accepted. Although each treats the cell as a homogeneous, incompressible, deformable sphere, only two consider explicitly the cortical region, treating it as a bounding membrane that exerts a small constant surface tension of order 30 pN/ $\mu\text{m}$ . In one model, the cell is treated as a linear standard viscoelastic solid (Schmid-Schönbein et al., 1981; Sung et al., 1988; Lipowsky et al., 1991), in another, as a Newtonian fluid bounded by constant surface tension (Evans and Yeung, 1989; Frank and Tsai, 1990; Needham and Hochmuth, 1990; Tran-Son-Tay et al., 1991; Hochmuth et al., 1993; Drury and Dembo, 1999), and in the last, as a linear Maxwell material, also bounded by constant surface tension (Dong et al., 1988; Skalak et al., 1990).

Of these three models, the Maxwell model with constant surface tension was selected for use in the present study. The model incorporates the elastic restoring effects of the actin-rich cortical layer lining the periphery of the cell, lying just below its external lipid bilayer, with the ability to capture both the elastic, solid-like short time-scale behavior of the cell and its viscous, fluid-like long time-scale behavior (Schmid-Schönbein et al., 1981; Evans and Kukan, 1984; Dong et al., 1988). Additionally, it is capable of predicting the experimentally observed linear compressive stroke force–displacement relation exhibited by neutrophils

during indentation, provided the material property values are appropriately chosen. Despite their predictive capabilities, the Newtonian model neglects cellular elasticity and predicts a concave downward force–displacement relation during indentation (Zahalak et al., 1990), and the standard solid model neglects the cell's cortical tension and predicts a static deformation limit to constant applied loads, in contradiction to the fluid-like behavior exhibited by neutrophils during micropipette aspiration (Evans and Yeung, 1989). We chose not to adopt one of the more recent inhomogeneous neutrophil models that treat the multi-lobed nucleus as a distinct entity from the cytoplasm (Tran-Son-Tay et al., 1998) due to their added complexity and because the limited amount of indentation data available to us precluded a unique determination of cytoplasmic and nuclear mechanical properties. Cortical shell bending effects were also neglected, because they have been shown in a micropipette aspiration study to be important only for very small pipette radii, less than 1  $\mu\text{m}$  (Zhelev et al., 1994).

Unlike nonstimulated neutrophils, for which numerous published models exist, fMLP-stimulated neutrophils have not been modeled extensively. For this reason, it was necessary to determine an appropriate model for fMLP-stimulated cells, and to determine appropriate model parameter values corresponding to various levels of stimulation. For consistency with the nonstimulated cell model, and due to its ability to accurately predict the force–displacement indentation data for fMLP-stimulated neutrophils, the Maxwell model with constant surface tension was also used to model the cell in its fMLP-stimulated state. Indentation experiments on nonstimulated and two levels of fMLP-stimulated neutrophils ( $10^{-9}$  and  $10^{-6}$  M) were simulated to determine their appropriate model parameter values (Worthen, et al., 1989).

For the nonstimulated neutrophil, a constant cortical tension of 31 pN/ $\mu\text{m}$  was assumed (Dong et al., 1988). For the fMLP-stimulated neutrophils, two assumptions regarding the effects of fMLP on neutrophil mechanical properties were made. First, the cortical tension of the cell was assumed to be unaffected by fMLP. Second, the characteristic viscoelastic decay time of the cell ( $\mu_{\text{cell}}/G_{\text{cell}}$ ) was assumed to be unaffected by fMLP concentration and equal to the value found for the nonstimulated cell,  $1/6$  s. The former assumption was made in the absence of quantitative information regarding the specific effects of fMLP on cortical tension, though it might be expected that cortical tension would increase in the presence of fMLP due to the high actin content of the cortical region and the fact that the primary effect of fMLP is to increase actin assembly (Worthen et al., 1989; Motosugi et al., 1996). (This is particularly the case when one considers that fMLP has been found to localize F-actin in the submembraneous region of circulating neutrophils [Saito et al., 2002] and that cytochalasin-D, which is known to disrupt actin filament organization, has been found to reduce cortical tension by

40–60% [Ting-Beall et al., 1995].) The latter assumption was made because we lacked an empirical basis for any other assumption, as might have been derived from the entire indentation force–displacement relation exhibited in studies of the type performed by Worthen et al., (1989).

### Mathematical model

The updated Lagrangian Hencky formulation was used to describe the kinematics of the neutrophil, accounting for the large displacements, rotations, and strains present in the model. The nonlinear kinematic formulation uses Cauchy stresses and their conjugate measure of deformation, Hencky (natural, logarithmic, or true) strains. For simplicity, we present here the Maxwell material constitutive law assuming small strain and small displacement conditions, and refer the reader to (K. J. Bathe, 1996) for details on how the extension is made to the fully nonlinear kinematic formulation used in the simulations.

We define the traceless stress deviator,  $\mathbf{T}'$ , representing the state of pure shear stress at a point as

$$\mathbf{T}' = \mathbf{T} - \frac{1}{3} T_{kk} \mathbf{I}, \quad (1)$$

where  $\mathbf{T}$  is the Cauchy stress tensor,  $\mathbf{I}$  is the identity tensor, and the summation convention is used. The traceless strain deviator,  $\mathbf{E}'$ , representing the state of pure shear strain at a point is defined as

$$\mathbf{E}' = \mathbf{E} - \frac{1}{3} E_{kk} \mathbf{I}, \quad (2)$$

where  $\mathbf{E}$  is the small strain tensor

$$\mathbf{E} = \frac{1}{2} [\tilde{\nabla} \mathbf{u} + (\tilde{\nabla} \mathbf{u})^T], \quad (3)$$

and  $\mathbf{u}$  is the material displacement vector.

Stress and strain in the homogeneous cell interior are related through the linear Maxwell constitutive law, written in differential form for the deviatoric response as

$$\frac{\mathbf{T}'}{2\mu_{\text{cell}}} + \frac{\dot{\mathbf{T}}'}{2G_{\text{cell}}} = \dot{\mathbf{E}}', \quad (4)$$

where  $\mu_{\text{cell}}$  is the constant coefficient of viscosity,  $G_{\text{cell}}$  is the constant elastic shear modulus, and a superimposed dot denotes time rate of change. Defining the mechanical pressure,  $p$ , to be the average compressive stress ( $p \equiv -1/3 T_{kk}$ ), the bulk response of a Maxwell material can be expressed as

$$p = -\kappa_{\text{cell}} E_{kk}, \quad (5)$$

where  $\kappa_{\text{cell}}$  is the bulk modulus. In this study, we assume that the cell is nearly incompressible, with a Poisson ratio of 0.499, so that the bulk modulus is related to the shear modulus by,  $\kappa_{\text{cell}} = 500G_{\text{cell}}$ .

The cortical layer lining the cell was modeled as a uniform thickness axisymmetric shell with constant in-plane equibiaxial tensile prestress (a two-dimensional state of

constant negative pressure). A linear elastic stress–strain law with a vanishingly small elastic modulus ( $E = 10^{-4}$  Pa) was chosen to model the constitutive behavior of the shell, and a very small shell thickness (1 nm) was assumed to ensure that bending and deformation-induced membrane effects on the response of the cell were negligible. These modeling assumptions approximated a constant, uniform surface tension bounding the cell that can be expressed as

$$\mathbf{n} \cdot \mathbf{T}^{(\text{cell})} \mathbf{n} = \mathbf{n} \cdot \mathbf{T}^{(\text{ext})} \mathbf{n} + 2H\gamma \quad \text{on } S_{\text{cell}}, \quad (6)$$

where  $S_{\text{cell}}$  denotes the cell's bounding surface,  $\mathbf{T}^{(\text{cell})}$  is the Cauchy stress tensor in the cell,  $\mathbf{T}^{(\text{ext})}$  is the Cauchy stress tensor in the body that is external to the cell (indenter or plasma),  $\mathbf{n}$  is the local outward-directed unit normal to the cell surface,  $\gamma$  denotes the constant coefficient of surface tension, and  $H$  denotes the mean local curvature of the cell surface, assumed positive when the center of curvature lies in the direction of the normal, and negative otherwise. The mean local curvature of the cell surface,  $H$ , can be expressed as the mean of the curvatures,  $1/R_1$  and  $1/R_2$ , of the surface in any two orthogonal planes containing the surface normal, where the curvatures have the same sign convention as  $H$ ,

$$H = \frac{1}{2} \left( \frac{1}{R_1} + \frac{1}{R_2} \right). \quad (7)$$

### Neutrophil indentation

The neutrophil-indentation model mimics the experimental study of Worthen et al., (1989) and is consistent with a previous finite-element simulation of the experiment (Zahalak et al., 1990). The experiment consisted of indenting individual neutrophils at a constant rate of indentation with a micrometer-scale glass rod (the indenter) and measuring the time course of the resultant force. During indentation, the cell was supported by a substrate that, like the indenter, was effectively rigid. The indentation experiments were conducted at room temperature using 30–82 cells from each of five donors, providing a statistical dataset for the neutrophil models to be based upon.

### Mathematical model

The undeformed cellular radius,  $R_{\text{cell}}$ , the indenter radius,  $R_{\text{indenter}}$ , and the radius of curvature of the indenter corner,  $\rho$ , (Fig. 1) have values of 4, 1, and 0.15  $\mu\text{m}$ , respectively. The axisymmetric equations of equilibrium used to integrate the time-dependent viscoelastic response of the cell can be written as

$$\text{div } \mathbf{T} = \mathbf{0}, \quad (8)$$

where we note that mass conservation was automatically satisfied by the use of a Lagrangian formulation.

Indentation velocity,  $\dot{\Delta}$ , was prescribed at the top center-most point of the indenter and corresponded to the experi-

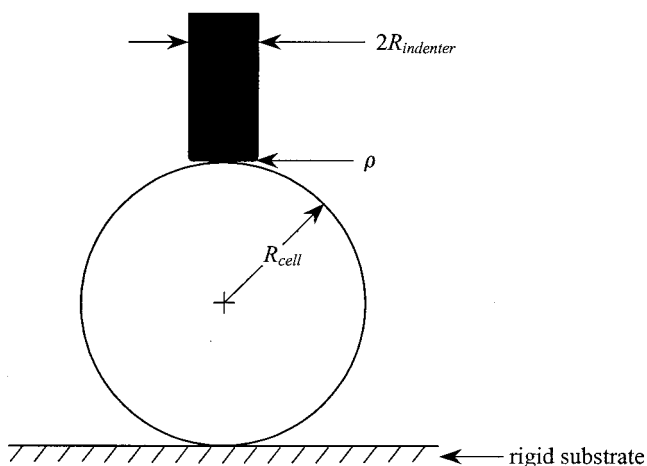


FIGURE 1 Initial configuration of indentation model: schematic of neutrophil, indenter, and substrate.

mental value of  $5.1 \mu\text{m/s}$ . Velocity was constant and equal in magnitude during the indentation and retraction strokes, and the indenter reached a maximum depth of  $\Delta_{\text{max}}$ , corresponding to  $1.5 \mu\text{m}$ . Although the experimental value of  $\Delta_{\text{max}}$  was  $2.2\text{--}2.6 \mu\text{m}$ ,  $1.5 \mu\text{m}$  was deemed sufficient for the simulations due to the linearity of the indenter force-displacement relationship during the downward, indentation stroke, observed both experimentally and numerically. Frictionless contact was assumed to occur between the indenter-cell and the substrate-cell surfaces, neglecting possible effects arising from biochemical adhesion. The kinematical contact condition satisfied at all times in the analysis by the

contacting bodies (ensuring impenetrability) can be expressed as

$$\mathbf{v}^{(\text{cell})} \cdot \mathbf{n} = \mathbf{v}^{(\text{ext})} \cdot \mathbf{n} \quad \text{on } S_{\text{contact}} \quad (9)$$

where  $\mathbf{v}^{(\text{cell})}$  is the material velocity of the cell,  $\mathbf{v}^{(\text{ext})}$  is the material velocity of the external, contacting body,  $\mathbf{n}$  is a unit vector normal to the contact surface, and  $S_{\text{contact}}$  is the relevant contact area, cell substrate or cell indenter. The normal stress jump present at the cell surface due to surface tension effects is as given in Eq. 6.

### Capillary transit

Pulmonary capillaries vary in radius from  $1$  to  $7.5 \mu\text{m}$  in humans, with a mean of  $3.7 \mu\text{m}$  (Doerschuk et al., 1993). They constitute a vast and complex network of interconnected segments, each of which is highly irregular in both cross-section and length, providing a formidable challenge from a modeling standpoint (Weibel, 1963). Because the primary aim of this study was to characterize the effects of capillary entrance geometry on neutrophil transit time, extending the relationship known for blunt-ended micropipette geometries (Yeung and Evans, 1989; Huang et al., 2001), and because we confined our analyses to rigid axisymmetric geometries, we modeled a typical capillary constriction as having a constant radius of curvature in the plane containing the vessel axis (the constriction radius of curvature is denoted  $a$  in Figs. 2 and 3). This approximation is one of many that could have been used, but it is well motivated by the geometric nature of pulmonary capillaries as exhibited in

FIGURE 2 SEM showing an interior view of the pulmonary capillaries in a rat lung, illustrating the motivation for modeling a typical capillary entrance as having a constant radius of curvature (labeled  $a$  above and in Fig. 3) (Reproduced by permission from Guntheroth et al., 1982).

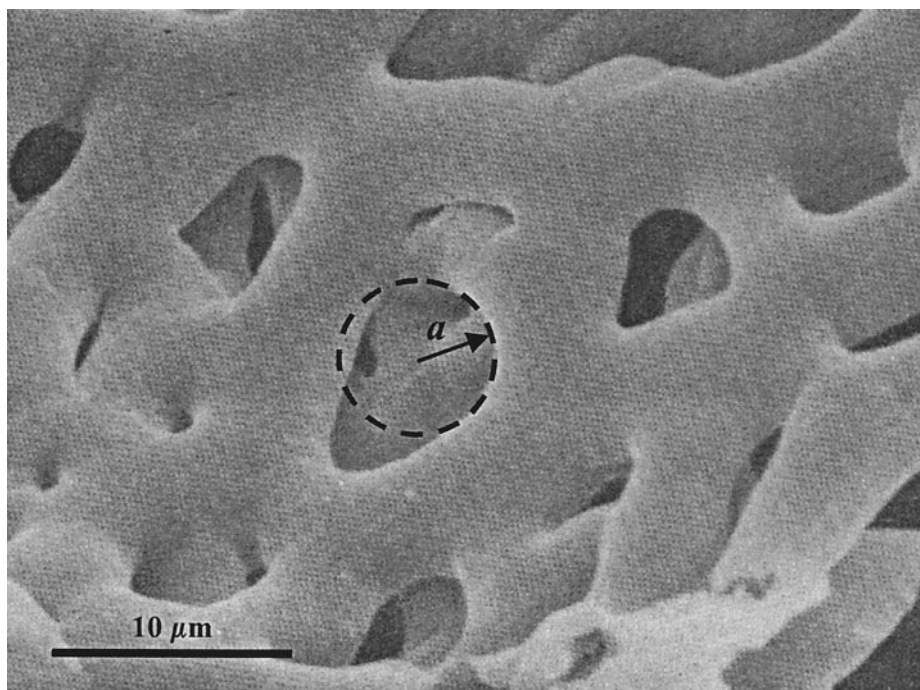
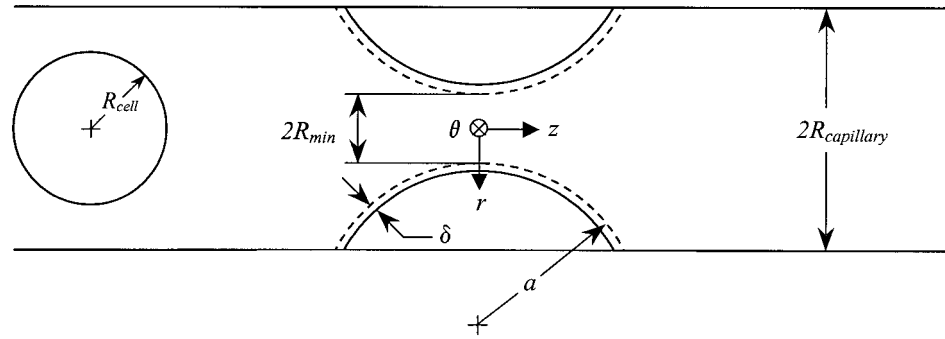




FIGURE 3 Schematic of the model capillary geometry with the cell in its initial, undeformed configuration (the cell is moving from left to right).



the micrograph shown in Fig. 2, where capillary cross-sections are seen to have entrance geometries that are reasonably well characterized by a constant radius of curvature.

It was also critical that we consider the glycocalyx. In the present model, the near-wall region is treated as a rigid layer, 100 nm thick and highly permeable to plasma. This is achieved by placing a frictionless contact surface 100 nm from the capillary wall. This assumption was made as a compromise between having no layer, in which case the neutrophil approaches to within several nanometers of the wall, and a representation of the glycocalyx as proposed in several recent models of red cell motion through capillaries (Pries et al., 1997; Damiano, 1998; Feng and Weinbaum, 2000). Note that, despite the recent progress made toward accurately modeling the glycocalyx, there is still considerable debate over the precise nature of the physical interaction between the glycocalyx and individual blood cells. Moreover, although it is likely that the pulmonary endothelium possesses a glycocalyx, to our knowledge it has not been directly observed and hence its thickness is unknown. Finally, although the thickness of the rigid layer used in our simulations was somewhat arbitrary, we numerically confirmed that the cellular transit times we obtained were independent of the specific value used within the range of 50 to 200 nm. The insensitivity of the cell's transit time to the layer thickness within this range is due to the facts that the pressure drop remained concentrated across the cell and the retarding shear stress imposed on the cell by the plasma in the layer region remained negligible (see Appendix).

*Mathematical model*

The axisymmetric capillary model is shown in Fig. 3, where the radii of curvature of the capillary wall and the contact surface are  $(a - \delta)$  and  $a$ , respectively, and the minimum constriction radius is  $R_{min}$ . The layer thickness, chosen to be 100 nm, is denoted  $\delta$ , and the unobstructed portions of the capillary were assumed to be cylindrical with radii  $R_{capillary}$ . Choosing the right-handed cylindrical coordinate system

$(r, \theta, z)$  shown in Fig 3, the contact surface constriction radius,  $R(z)$ , can be expressed analytically as

$$R(z) = (R_{min} + a) - \sqrt{a^2 - z^2} \quad \text{for } (-l \leq z \leq l), \quad (10)$$

where  $z$  denotes position along the capillary axis, and  $l$  is the axial half-length of the contact surface. The upstream and downstream straight sections of the capillary model were chosen to be between 8–15 and 23–26 $R_{cell}$ , respectively.

The dynamical equations of motion were solved incrementally in time for both the cell and plasma, in a fully coupled manner. For the cell, the equations of motion are expressed in Lagrangian form as

$$\rho_{cell} \frac{D\mathbf{v}}{Dt} = \text{div } \mathbf{T}, \quad (11)$$

where  $\rho_{cell}$  is the constant cell density and the operator  $D/Dt$  denotes material time rate of change. For the plasma, the equations of motion are expressed in Arbitrary Lagrangian–Eulerian (ALE) form (K. J. Bathe et al., 1995). The ALE formulation was needed to maintain the integrity of the finite element mesh in the plasma domain as the cell underwent large displacements through the capillary constriction. In the ALE formulation, the equations of motion are expressed as

$$\rho_{plasma} \left( \frac{\delta \mathbf{v}}{\delta t} + (\mathbf{v} - \mathbf{v}_m) \cdot \text{grad } \mathbf{v} \right) = \text{div } \mathbf{T}, \quad (12)$$

where  $\rho_{plasma}$  is the constant plasma density,  $\mathbf{v}_m$  is the mesh velocity,  $\delta \mathbf{v} / \delta t$  is the time rate of change of the plasma velocity as measured at a moving mesh point, and all velocities are measured with respect to an inertial frame of reference. The equation of continuity for the plasma, treated as an incompressible, Newtonian fluid with viscosity  $\mu_{plasma}$ , can be expressed as

$$\text{div } \mathbf{v} = 0. \quad (13)$$

For the plasma, a kinematical condition of no-slip was assumed on the rigid capillary wall,

$$\mathbf{v} = \mathbf{0} \quad \text{on } S_{capillary}, \quad (14)$$

and constant normal tractions were applied on the plasma at the capillary inlet and outlet

$$\mathbf{Tn} = t_{\text{inlet}} \mathbf{n} \quad \text{on} \quad S_{\text{inlet}}, \quad (15)$$

$$\mathbf{Tn} = t_{\text{outlet}} \mathbf{n} \quad \text{on} \quad S_{\text{outlet}}, \quad (16)$$

where  $t_{\text{inlet}}$  and  $t_{\text{outlet}}$  are the magnitudes of the prescribed inlet and outlet traction vectors, respectively. Fully developed flow at the inlet and outlet of the model resulted in the fluid pressure being equal to the applied normal tractions, and hence the total pressure drop across the capillary model, denoted  $\Delta P$ , was simply equal to the difference between the normal traction values. Trans-capillary pressure drop was assumed to vary between the physiological values of 20 and 80 Pa (Huang et al., 2001) and, although the very low Reynolds number of the flow ensured that inertial effects were negligible, the inertial terms were retained in the momentum equations solely for numerical purposes.

Velocity and shear stress continuity were satisfied at the cell–plasma interface throughout the analysis, whereas there was a jump in the normal stress between the cell and plasma due to the effects of surface tension, as expressed earlier in Eq. 6.

When the cell enters the constriction, a portion of its surface contacts the capillary-constriction contact surface used to model cellular interactions with the glycocalyx (Fig. 3). While in contact, an additional normal traction is applied to the cell to ensure that the gap between the contact surface and capillary wall remains constant and equal to  $\delta$ . During this time, the normal contact traction applied to the cell by the contact surface is superimposed upon the traction vector exerted onto the cell by the plasma (which generally consists of normal and shear components), so that a force balance is maintained at the cell–plasma–contact–surface interface.

### Dimensional analysis

The transit time,  $T$ , required for the model cell to transit through the capillary constriction can be expressed in its most general form as a function of all the dimensional parameters in the model,

$$T = f(R_{\text{cell}}, G_{\text{cell}}, \mu_{\text{cell}}, \gamma, R_{\text{capillary}}, R_{\text{min}}, a, \delta, \mu_{\text{plasma}}, \Delta P), \quad (17)$$

where  $T$  is defined as the time from which the leading edge of the cell crosses the capillary constriction inlet to the time when the trailing edge of the cell crosses the capillary constriction outlet. To reduce the number of independent dimensional parameters in Eq. 17, several simplifying assumptions are made. First, it is assumed that  $T$  will be nearly independent of the upstream and downstream capillary radius,  $R_{\text{capillary}}$ , provided that  $T \gg \tau_{\text{conv}}$ , where  $\tau_{\text{conv}}$  is the convective time scale of the cell when it is freely traveling

in the capillary ( $\sim R_{\text{cell}}/\bar{V}$ , where  $\bar{V}$  is the average plasma velocity in the unconstricted capillary). In this limit, the bulk of the transit time consists of the time spent by the cell squeezing through the capillary constriction, during which the constant pressure drop is applied across the cell, and is independent of the upstream and downstream capillary radii. Second, it is assumed that in the same limit, the capillary transit time will be insensitive to variations in plasma viscosity,  $\mu_{\text{plasma}}$ , and gap thickness,  $\delta$ , between the constriction contact surface and the wall. As the cell squeezes through the constriction, there are only two retarding forces balancing the axial pressure gradient: one is due to the axial component of the normal contact traction applied to the cell by the constriction contact surface and the other is due to the Couette component of the shear stress in the gap. As shown in the Appendix, for the parameter ranges explored in this study, the retarding force due to the Couette flow-induced shear stress is negligible, validating the assumption that the transit time is independent of  $\mu_{\text{plasma}}$  and  $\delta$ . Finally, we have excluded the upstream and downstream lengths of the capillary model from the transit time expression because viscous losses in those regions were negligible during transit. Thus, the applied trans-capillary pressure drop ( $\Delta P$ ) remained concentrated across the cell independently of their specific lengths, within the range provided in the mathematical model section.

Using the above arguments, the number of independent variables in the dimensional transit time equation above (Eq. 17) is reduced to seven,

$$T = g(R_{\text{cell}}, G_{\text{cell}}, \mu_{\text{cell}}, R_{\text{min}}, a, \Delta P, \gamma). \quad (18)$$

Choosing  $\mu_{\text{cell}}/\Delta P$  as the characteristic time scale, the dimensional transit time equation can be written in dimensionless form as

$$T^* = h(G^*, R^*, a^*, \gamma^*), \quad (19)$$

where  $T^* \equiv (T\Delta P/\mu_{\text{cell}})$ ,  $G^* \equiv (G_{\text{cell}}/\Delta P)$ ,  $R^* \equiv (R_{\text{min}}/R_{\text{cell}})$ ,  $a^* \equiv (a/R_{\text{cell}})$ , and  $\gamma^* \equiv [\gamma/(\Delta PR_{\text{min}})]$  measures the effects of the bounding surface tension on reducing the effective pressure drop driving the cell into the constriction.

## NUMERICAL SOLUTION OF THE GOVERNING EQUATIONS

Solutions of the nonlinear governing equations for the indentation and capillary flow models presented in the previous sections were obtained using a commercially available finite element program (ADINA, Version 7.5, Watertown, MA).

### Finite element formulation

The cell interior was discretized in space with 4/1 quadrilateral axisymmetric mixed (u/p) solid elements. The ele-

ments use bilinear displacement interpolation and a constant pressure degree of freedom to analyze effectively nearly incompressible media (Sussman and Bathe, 1987). Two-node axisymmetric shell elements were used to discretize the cortical region bounding the cell, with two displacement and one rotation degree of freedom per node, consistent with the bilinear elements used for the cell interior. Surface tension effects were modeled by imposing an initial state of uniform biaxial stress on the shell elements (see Modeling: The neutrophil).

The updated Lagrangian Hencky kinematic formulation was used to analyze the cellular response in both the indentation and capillary flow models, and the constraint function method was used to satisfy the nonlinear contact conditions (K. J. Bathe, 1996). Temporal discretization of the finite element equations used the Newmark method for the indentation simulations and the Euler backward method for the fluid–solid interaction (cell–capillary) simulations.

Three-node triangular axisymmetric elements were used for spatial discretization of the plasma. The elements interpolate pressure and velocities linearly and use an additional bubble function for the velocities. Both the fluid and solid elements satisfy the inf–sup (infimum–supremum) or Babuška-Brezzi condition for stability and optimality in nearly or exactly incompressible analysis (Brezzi and Fortin, 1991).

Numerical solution of the governing solid and fluid equations of the capillary model required the use of the fluid–solid interaction analysis capabilities of ADINA (Rugonyi and K. J. Bathe, 2001). The solution obtained was fully coupled in the sense that the kinematical conditions of displacement, velocity, and acceleration continuity across the no-slip fluid–solid (cell–plasma) interface were satisfied at all times during the analysis, and the conditions of shear stress continuity and normal stress discontinuity due to surface tension effects presented in the previous section.

Computations were performed on Silicon Graphics Incorporated Origin and Octane workstations on single 300-MHz CPUs. Memory requirements were minimal because the models were two-dimensional. CPU times varied depending upon the model type and the temporal and spatial discretizations used, but generally were between 10–15 min and 1.5–2 h for the indentation and capillary flow models, respectively. We note that convergence difficulties were encountered during the final, exit phase of the capillary flow simulations due to the large acceleration of the cell during that time.

### Finite element solution validation

Validation of the finite element results consisted of two parts. First, mesh and time-step refinements were performed to ensure convergence of the results to the solution of the underlying continuum models (see Modeling). It was verified that the solution variables of interest (indentation force

and cell transit time for the indentation and capillary flow models, respectively) changed by less than 5% when the spatial density of nodes was doubled in the solid and fluid models and when the time-step size was halved. Second, to further validate the methods used in the neutrophil–capillary analysis, we simulated a problem similar to one previously analyzed by Tran-son-tay et al. (1994). In that study, the authors simulated the flow of a Newtonian droplet with surface tension through a converging tapered tube in an effort to model the flow of a neutrophil through a tapered glass capillary tube. In what follows, we present a brief overview of the tapered tube model along with a results comparison, and refer the reader to Tran-son-tay et al. (1994) for details of the original study.

### Tapered tube model

The original tapered tube model of Tran-son-tay et al. consists of a highly viscous Newtonian droplet of viscosity,  $\mu$ , bounded by constant surface tension,  $\gamma$ , flowing through an axisymmetric tube of constant converging half-angle,  $\alpha$ , under a constant driving pressure drop,  $\Delta P$ . The original droplet diameter is denoted  $D_0$  and the deformed axial end-to-end length of the droplet  $L$ . In their model, the external fluid is assumed to be inviscid, resulting in a uniform pressure applied to the droplet at its upstream and downstream ends and zero shear stress acting along its conical section (within the gap). Lastly, a time-varying normal pressure is applied along the conical section of the droplet to satisfy axial equilibrium, and the normal component of the droplet velocity is constrained to be zero there to satisfy the geometric constraint imposed by the wall. The axisymmetric creeping-flow equations are solved numerically in time employing the methods used earlier by Yeung and Evans (1989) to study neutrophil aspiration into glass micropipettes.

In the present study, we simulate these conditions employing the same methods as those used for the capillary flow model (*see Capillary Transit*,) changing the geometry to be that of the tapered tube. The gap thickness and external fluid viscosity are chosen such that the retarding shear stress on the droplet is negligible and the pressure drop applied across the ends of the tapered tube is concentrated across the droplet. The ratio of external to internal viscosity was  $\mu_{\text{ext}}/\mu = 10^{-6}$  and the dimensionless gap thickness was  $\delta/D_0 = 0.015$ . We simulate the droplet's Newtonian constitutive response by choosing the elastic shear modulus of the Maxwell droplet to be 1000 times the driving pressure drop ( $G^* \gg 1$ ), ensuring that elastic deformations are negligible. Though the zero wall shear-stress assumption is satisfied along the conical section of the droplet due to the low viscosity of the external fluid, no assumption is made as to the form of the wall (contact) normal stress distribution acting on the droplet. The relevant dimensionless model

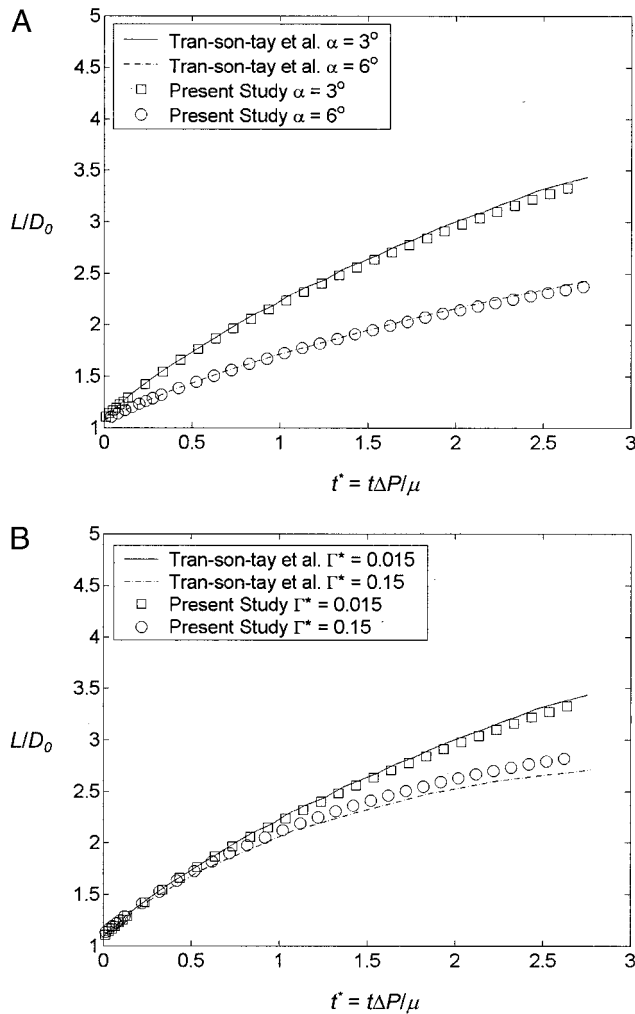


FIGURE 4 Comparison between the tapered tube results of Tran-Son-Tay et al. (1994) and the present study illustrating (A) the effects of taper angle on droplet entry rate ( $\Gamma^* = 0.015$ ;  $\alpha = 3^\circ, 6^\circ$ ) and (B) the effects of surface tension on entry rate ( $\alpha = 3^\circ$ ;  $\Gamma^* = 0.015, 0.15$ ).

parameters are time,  $t^* = t\Delta P/\mu$ , surface tension  $\Gamma^* = \gamma/(\Delta PD_0)$ , and droplet end-to-end length,  $L/D_0$ .

#### Tapered tube results

Three model conditions ( $\Gamma^* = 0.015$ ,  $\alpha = 3^\circ$ ;  $\Gamma^* = 0.015$ ,  $\alpha = 6^\circ$ ; and  $\Gamma^* = 0.15$ ,  $\alpha = 3^\circ$ ) were analyzed in the original study to illustrate the effects of taper angle and surface tension on entry rate, and each is simulated here for validation. The entry rate of the droplet decreases sharply with increasing taper angle from  $3^\circ$  to  $6^\circ$ , while  $\Gamma^*$  is held constant at 0.015 (Fig. 4 A), the effects being significant even for small deformations ( $L/D_0 \rightarrow 1$ ). Increasing surface tension by a factor of 10 from  $\Gamma^* = 0.015$  to 0.15 while  $\alpha$  is held constant at  $3^\circ$  (Fig. 4 B) is seen to have the opposite effect, namely to decrease entry rate (due to the reduction in effective driving pressure caused by the different radii of

curvature at the leading and trailing ends). Differences are  $<5\%$  even at the time of maximum deformation ( $t^* = 2.7$ ) and attributable to differences in the underlying mathematical models and the numerical methods used to solve them.

## RESULTS

### Neutrophil indentation

The objective of the indentation simulations was to determine appropriate Maxwell model parameter values for the neutrophil in its nonstimulated state and after stimulation with two concentrations of fMLP that induce neutrophil activation. Instantaneous finite-element mesh configurations of the deformed, nonstimulated cell model are shown superimposed upon the original, undeformed mesh at two times: when the cell is maximally indented to  $1.5 \mu\text{m}$  (0.294 s) (Fig. 5 A) and at the instant when the indenter is returned to its original, zero displacement position (0.588 s) (Fig. 5 B). Note that the cell remains significantly deformed even after the indenter has returned to its original position. The reasons for this are twofold. First, the viscoelastic relaxation time scale of the cell [ $\tau_{\text{relax}} \sim (\mu_{\text{cell}}/G_{\text{cell}}) = 0.167 \text{ s}$ ] is on the order of the indentation time scale [ $\tau_{\text{indent}} \sim (\Delta_{\text{max}}/\dot{\Delta}) = 0.294 \text{ s}$ ], so that much of the work done by the indenter is dissipated in the cell during indentation, rather than elastically stored and transmitted back to the indenter during retraction. Second, the cell-recovery time scale [ $\tau_{\text{recovery}} \sim (\mu_{\text{cell}}R_{\text{cell}}/\gamma) = 3.97 \text{ s}$ ] is long compared to the indentation time scale, meaning that the surface tension force is too small to restore the cell to its spherical shape in the time it takes the indenter to retract.

The Maxwell model parameters,  $G_{\text{cell}}$  and  $\mu_{\text{cell}}$ , determined by the cell indentation simulations are listed in Table 1 for each level of fMLP stimulation, and the force–displacement curves computed with each model are compared with the experimental results in Fig. 6. The indentation force–displacement relationship is nearly linear in all cases, and significant hysteresis is exhibited as the indenter is withdrawn. The effects of fMLP on cellular viscosity and shear modulus are significant (Table 1), purportedly due to increased actin assembly (Worthen et al., 1989). Viscosity varies from a low of 30.8 Pa·s in the nonstimulated case to 225 Pa·s in the maximally stimulated case, while the cell's shear modulus increases from 185 to 1350 Pa.

### Capillary flow

The indentation results can be used with the modeling data presented (see Modeling) to define physiologically relevant dimensional and dimensionless parameter ranges for the capillary flow simulations. Considering that  $R_{\text{min}}$  ranged between 2.5 and  $3 \mu\text{m}$ ,  $a$  varied between about 8 and  $180 \mu\text{m}$ ,  $\Delta P$  ranged from 20 to 80 Pa,  $\gamma$  was equal to  $31 \text{ pN}/\mu\text{m}$ ,  $G$  ranged from 185 to 1350 Pa, and  $R_{\text{cell}}$  was assumed to be



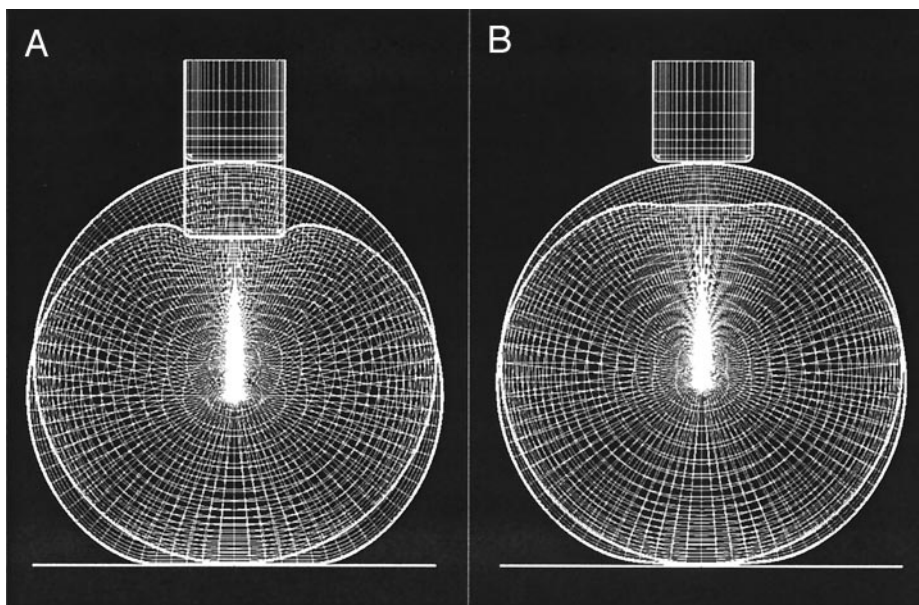


FIGURE 5 Superimposed depictions of the indentation model (nonstimulated cell) in its original and two deformed configurations, corresponding to (A) the time of maximum indentation ( $t = 0.294$  s) and (B) the instant when the indenter returns to its original, zero-displacement position after indentation ( $t = 0.588$  s).

4  $\mu\text{m}$ , the following dimensionless parameter ranges of interest are determined

$$\begin{aligned} 2 &\leq G^* \leq 70, \\ 0.625 &\leq R^* \leq 0.75, \\ 2 &\leq a^* \leq 45, \\ 0.13 &\leq \gamma^* \leq 0.62. \end{aligned} \tag{20}$$

In carrying out the simulations,  $\gamma^*$  was fixed in the narrower range of  $0.26 < \gamma^* < 0.31$  (corresponding to the physiological values of  $\Delta P = 40$  Pa,  $\gamma = 31$  pN/ $\mu\text{m}$ , and  $R_{\text{min}} = 2.5\text{--}3$   $\mu\text{m}$ ). To reduce the total parameter space spanned. This modeling assumption is justified by the following observations. First, we found that the effects of  $\gamma^*$  on the cell's transit time were significant only for the smallest  $a^*$  and  $R^*$  due to the relatively mild deformations incurred in this study (for example, in the extreme constriction case of  $R^* = 0.625$ , increasing  $\gamma^*$  by more than ten-fold from 0.04 to 0.62 increased the transit time by 22% for  $a^* = 2.19$ , whereas it increased the transit time by only 7% for  $a^* = 44.2$ ). Second, we found that the effects of  $\gamma^*$  on reducing the effective driving pressure drop cannot be

accounted for by the simple expression,  $\Delta P_{\text{eff}} = \Delta P - \Delta P_{\text{crit}} = \Delta P - 2\gamma[(1/R_{\text{min}}) - (1/R_{\text{cell}})]$ , applicable to micropipette aspiration (Evans and Yeung, 1989). The reason is that during flow into the capillary constrictions analyzed here, the radii of curvature of the leading and trailing end caps of the cell change continuously, whereas, in micropipette aspiration, they remain approximately constant (particularly the leading radius of curvature interior to the pipette) for the duration of flow. For these reasons, we

**TABLE 1** Nonstimulated and fMLP-stimulated neutrophil model parameters determined from indentation

fMLP Concentration (M)	Experimental Indentation Stiffness (nN/ $\mu\text{m}$ )	$G_{\text{cell}}$ (Pa)	$\mu_{\text{cell}}$ (Pa·s)	$\gamma$ (pN/ $\mu\text{m}$ )
0	0.540	185	30.8	31
$1 \times 10^{-9}$	1.65	625	104	31
$1 \times 10^{-6}$	3.48	$1.35 \times 10^3$	225	31

Indentation stiffness is defined as the slope of the linear, compressive portion of the force–displacement curve.

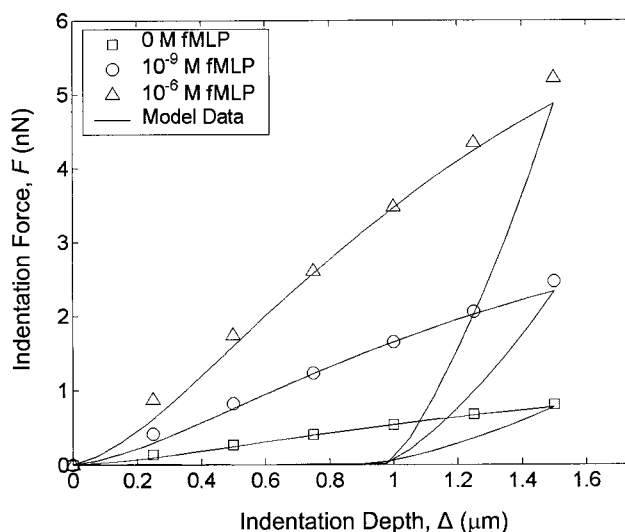


FIGURE 6 Maxwell model fit to mean experimental indentation data for nonstimulated,  $1 \times 10^{-9}$  M fMLP-stimulated, and  $1 \times 10^{-6}$  M fMLP-stimulated neutrophils incubated at room temperature. Symbols, experimental data from Worthen et al. (1989); solid lines, finite element model results. Mean experimental indentation force–displacement slopes (or stiffnesses) and best-fit Maxwell model parameter values are listed in Table 1.

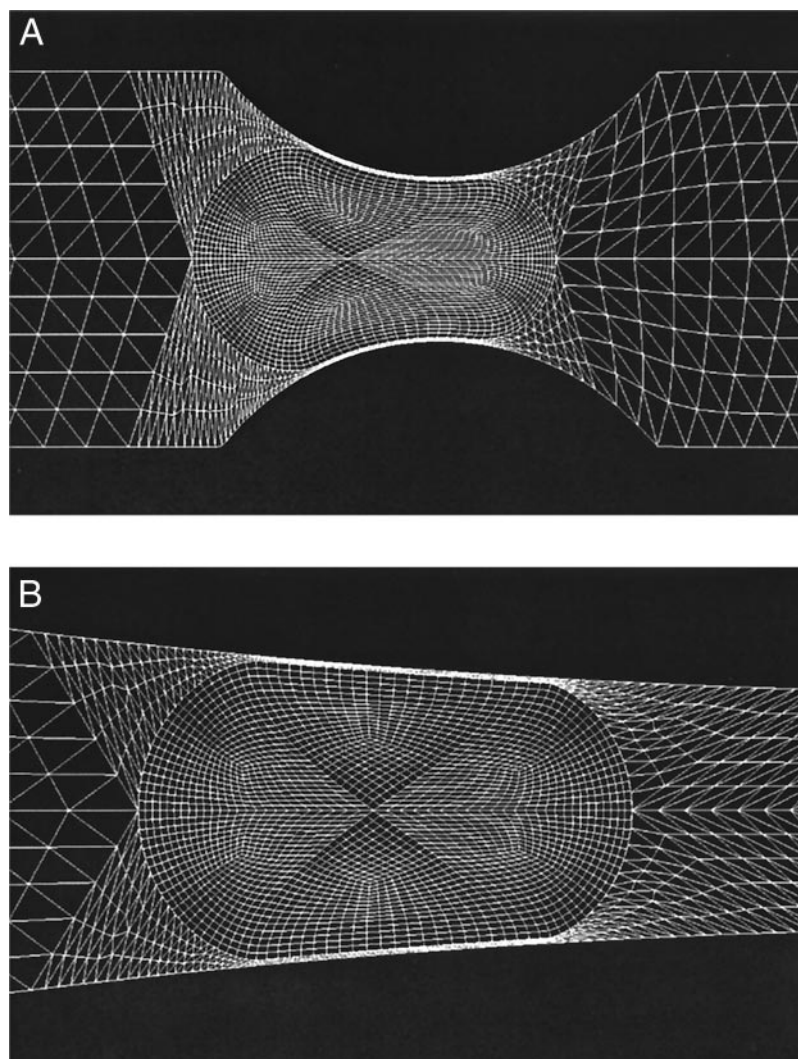


FIGURE 7 Typical deformed mesh configurations of the cell ( $G^* = 80$ ) entering two model capillary constrictions with the same minimum constriction radii ( $R^* = 0.625$ ) but different constriction radii of curvature, corresponding to (A)  $a^* = 2.19$  and (B)  $a^* = 44.2$ . The cell is moving from left to right.

chose to investigate the dependence of  $T^*$  on  $a^*$ ,  $R^*$ , and  $G^*$  for the physiologically relevant range of  $\gamma^*$  specified above, as a compromise between practicality (limiting the number of simulations required) and the lack of a simple expression to account for the effects of surface tension on the characteristic time scale  $\mu_{\text{cell}}/\Delta P$ . We also note that the lower bound on  $R^*$  is decreased to 0.50 only for the viscous deformation-dominated limit  $G^* \gg 1$ , to broaden the scope of the study; the minimum value of  $G^*$  had to be increased from 2 to 8 due to convergence difficulties; and that  $\mu_{\text{cell}}$  does not appear in the independent dimensionless groups because it is only used to scale  $T$ .

Typical deformed finite-element mesh configurations of two different cell–capillary models are depicted in Fig. 7. In each case  $G^* = 80$  and  $R^* = 0.625$ . The models differ only in that  $a^* = 2.19$  and 44.2 in Fig. 7 A and B respectively. Although the entire capillary constriction is visible in Fig. 7 A due to the small constriction radius of curvature, only a

small region of the constriction is visible in Fig. 7 B due to its large radius of curvature. In each model, the portions of the cell that are internal and external to the capillary constriction are nearly spherical, as expected due to the effects of surface tension.

For each value of  $R^*$  and  $a^*$  analyzed,  $T^*$  exhibits a clear limiting behavior with respect to  $G^*$  (Fig. 8 A, B, and C). In each case,  $T^*$  reaches a plateau for large  $G^*$ , the transition occurring in the vicinity of  $G^* \approx 20$ . The limiting behavior represents the parameter range in which the shear modulus of the cell is significantly greater than the driving pressure drop, so that the Maxwell model behaves essentially as a purely Newtonian fluid (i.e., elastic deformation during transit is negligible compared to total viscous deformation). For  $G^* < 20$ , however, elastic deformation of the cell becomes significant and the reduction in transit time grows sharply as  $G^* \rightarrow 0$ , particularly in the mildest constriction case (Fig. 8 A,  $R^* = 0.75$ ). This result is intuitive because

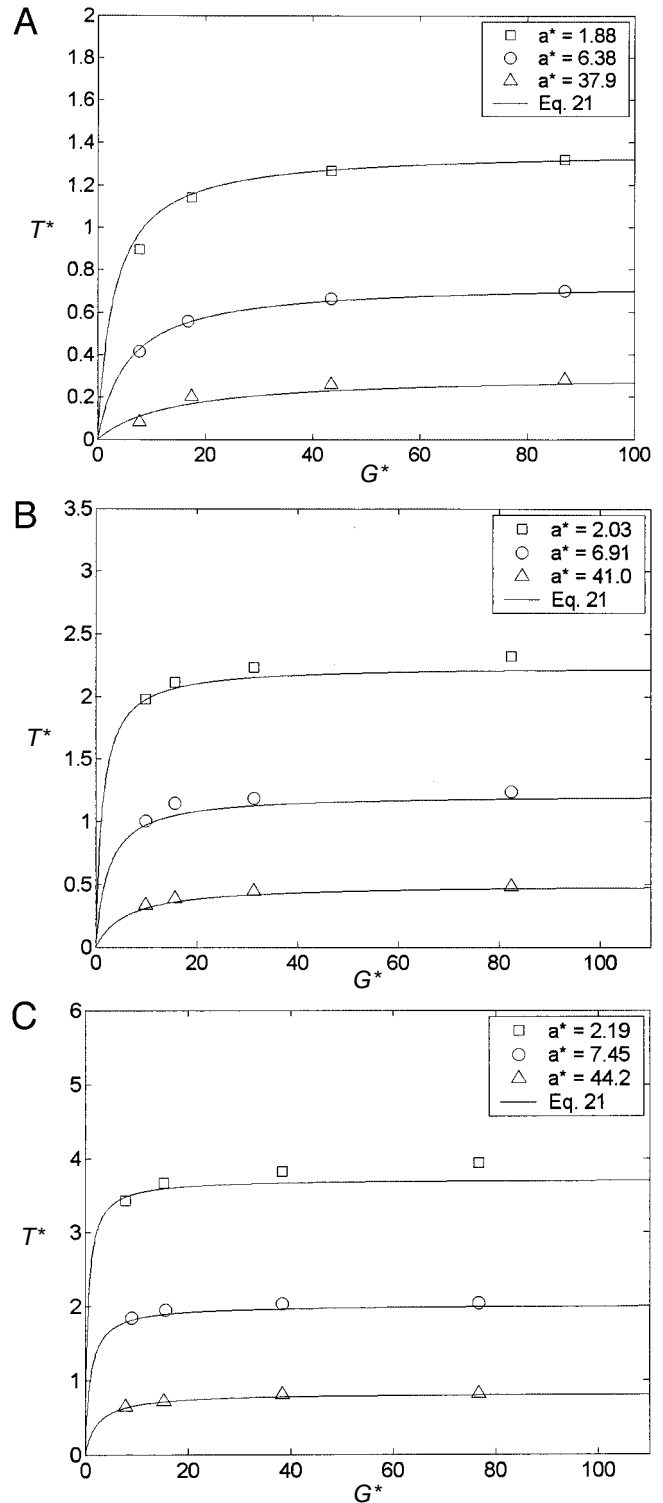


FIGURE 8 Dimensionless cell transit time,  $T^* \equiv [T\Delta p/\mu_{\text{cell}}]$ , versus dimensionless cell elastic shear modulus,  $G^* \equiv [G_{\text{cell}}/\Delta p]$ , for dimensionless minimum constriction radii, (A)  $R^* \equiv (R_{\text{min}}/R_{\text{cell}}) = 0.75$ , (B)  $R^* = 0.6875$ , and (C)  $R^* = 0.625$ , and three constriction radii of curvature,  $a^* \equiv (a/R_{\text{cell}})$ . Comparison between numerical results (*symbols*) and Eq. 21 (*curves*).

in the limit of small  $G^*$  and  $R^*$  approaching one, the cell will flow through the constriction purely elastically, without any viscous deformation at all. Although  $T^*$  depends strongly on  $R^*$ , it also exhibits a significant dependence on  $a^*$  for all values of  $R^*$  simulated (Fig. 8, A, B, and C).

Additionally, the dependence of  $T^*$  on  $a^*$  appears to be independent of  $G^*$  in the viscous deformation-dominated limit  $G^* \gg 1$ .

Within the approximate range of parameter values specified by Eq. 20, the following dimensionless rela-

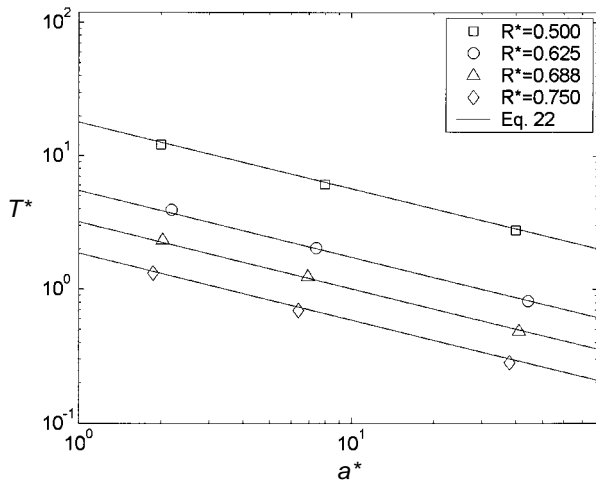


FIGURE 9 The dependence of dimensionless transit time,  $T^*$ , on dimensionless constriction radius of curvature,  $a^*$ , and minimum constriction radius,  $R^*$ , for the viscous deformation dominant regime ( $G^* \gg 1$ ). Data points are from the viscous limit simulations ( $G^* = 80$ ) and lines are produced from Eq. 22.

relationship was found to fit the data ( $R^2 = 0.997$ ) (Fig. 8 A, B, and C)

$$T^* = 0.58(a^*)^{-0.50} [(R^*)^{-5.0} - 1] \times \left( \frac{(a^*)^{-0.50} G^*}{40(R^*)^{10} + (a^*)^{-0.50} G^*} \right). \quad (21)$$

In light of the observation that  $T^*$  becomes independent of  $G^*$  for  $G^* \gg 1$ , we now focus on this (Newtonian) regime, in which the relation for  $T^*$  (Eq. 21) simplifies to ( $R^2 = 0.997$ ),

$$T^* = 0.58(a^*)^{-0.50} [(R^*)^{-5.0} - 1]. \quad (22)$$

Figure 9 illustrates the computed dependence of  $T^*$  on  $R^*$  and  $a^*$ , where each simulation data point has been obtained from the maximum  $G^*$  data point shown in Fig. 8, and, as noted earlier, additional data have been generated to represent the case of  $R^* = 0.50$ .

Though the transit time expressions (Eqs. 21 and 22) fit the simulation data within the ranges of the dimensionless parameters given in Eq. 20, in the limit as  $a^* \rightarrow 0$ , corresponding to a “sudden contraction” capillary geometry, Eqs. 21 and 22 suggest that  $T^*$  increases without bound, a result that is clearly in error.  $T^*$  must exhibit a limiting behavior well before the singular limit of  $a^* = 0$ . Although the precise value of  $a^*$  at which this transition takes place is not currently known, scaling arguments would point to a value on the order of one, when the constriction radius of curvature is equal to the cellular radius. This result is confirmed by the agreement between the analytical transit time relationship derived by Huang et al. for the flow of a Newtonian droplet into a micropipette and Eq. 22 for  $a^* = 1$  shown in Fig. 10. Note that, in Fig. 10, we compare  $T^* = T\Delta P/\mu_{\text{cell}}$

of Eq. 22, which is strictly only valid for  $0.26 < \gamma^* < 0.31$ , with  $T^*_{\text{pipette}} = T\Delta P_{\text{eff}}/\mu_{\text{cell}}$  of the micropipette aspiration model, which, as mentioned earlier, analytically accounts for the effects of  $\gamma$  on the transit (or aspiration) time by defining an effective driving pressure drop,  $\Delta P_{\text{eff}} \equiv \Delta P - 2\gamma[(1/R_{\text{min}}) - (1/R_{\text{cell}})]$  (Yeung and Evans, 1989). This leads us to further observe that, for the micropipette limit, the effect of  $\gamma$  on  $T$  is explicitly known, and that there exists a critical pressure drop,  $\Delta P_{\text{crit}} = 2\gamma[(1/R_{\text{min}}) - (1/R_{\text{cell}})]$ , below which  $T$  becomes infinite. Although a similar critical pressure drop must exist for the capillary model analyzed here, it is complicated by the different geometry and cannot be described by such a simple algebraic expression. We can say, however, that the critical pressure drop in our gradual entrance geometry will be less than the corresponding value in a micropipette, because the external radius of curvature will be  $\leq R_{\text{cell}}$ .

## DISCUSSION

In this study, we analyze neutrophil transit through individual capillary segments in the pulmonary microvascular network and present several new results. First, we have demonstrated that a Maxwell model with constant bounding surface tension is capable of reproducing the mechanical behavior of neutrophils not only during micropipette aspiration (Dong et al., 1988; Skalak et al., 1990), but also during experiments of neutrophil indentation. Second, the magnitude of the changes in cellular mechanical properties resulting from various levels of fMLP-stimulation has been estimated using the model. Finally, in an independent series

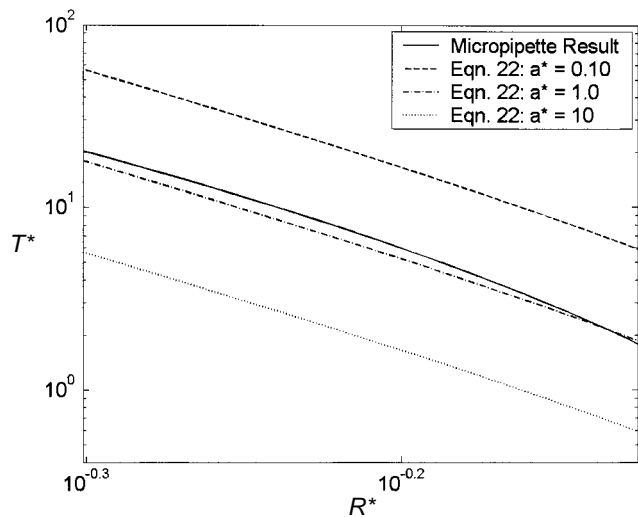


FIGURE 10 Comparison between the Newtonian limit ( $G^* \gg 1$ ) transit time expression of this study (Eq. 22) for  $a^* = 1$  and the micropipette aspiration time expression for a Newtonian droplet with surface tension (Eq. 41 from Huang et al., 2001), indicates that the capillary model transit time expressions presented in this study lose their dependence on  $a^*$  when  $a^* \leq 1$ .



**TABLE 2** Published neutrophil viscosity values for small deformation, nonstimulated neutrophil studies performed at room temperature

Reference	Viscosity (Pa·s)	Model
Schmid-Schönbein et al., 1981	6.5	Standard solid
Sung et al., 1988	17	Standard solid
Dong et al., 1991	18	Maxwell
Dong et al., 1988	30	Maxwell
Hochmuth et al., 1993	60	Newtonian
Frank and Tsai, 1990	89	Newtonian
Present Study	31	Maxwell

of simulations, we have used the model to examine the importance of radius of curvature at the entrance to a capillary segment on neutrophil transit time and found it to be a critical factor. Simple algebraic expressions were derived that fit the numerical predictions over a wide range of parameter values. Future studies of neutrophil transit will need to take entrance geometry into account if accurate estimates are to be made. Taken together, these results suggest that a Maxwell model is capable of capturing neutrophil mechanics under a variety of deformations, and that such models can be useful in calculating capillary transit times provided capillary geometry is adequately described.

## The neutrophil model

### Comparison to previous studies

Nonstimulated neutrophil response has been studied intensively during the past two decades (Schmid-Schönbein et al., 1981; Dong et al., 1988; Evans and Yeung, 1989; Needham and Hochmuth, 1990; Zahalak et al., 1990; Lipowsky et al., 1991; Skalak et al., 1990; Tran-Son-Tay et al., 1991; Warnke and Skalak, 1992; Tsai et al., 1993; Zhelev et al., 1994; Drury and Dembo, 1999) primarily using micropipette aspiration and recovery techniques (incurring small and large deformations, imposing high and low rates of deformation, and using small and large pipettes) in conjunction with analytical and numerical methods to determine appropriate neutrophil models and their parameter values. Although the range in viscosities found in small deformation studies (Table 2) is quite significant (6.5 to 89 Pa·s), the nonstimulated cellular viscosity found in the present study using indentation (30.8 Pa·s) is seen to be in good agreement. Studies using the Maxwell model with cortical tension have reported nonstimulated cellular shear moduli as low as 28.5 Pa (Dong et al., 1988) for very small deformations and as high as 250 Pa (Dong and Skalak, 1992) for larger deformations ( $R_{\min}/R_{\text{cell}} = 0.5$ ), bracketing our result of 185 Pa. Zahalak et al., (1990) studied the mechanical response of nonstimulated and fMLP-stimulated neutrophils using a finite element model of the same experimental indentation data that this study is based on, though they

neglected viscous effects in treating the cells as purely elastic. They found that treatment with  $10^{-8}$  M fMLP resulted in an increase in cellular shear modulus of almost a factor of four, from 118 to 448 Pa, in reasonable agreement with the results of the present study (Table 1). Only one study with which we are familiar quantified the effects of fMLP both on leukocyte viscosity and shear modulus (Lipowsky et al., 1991), finding that topical application ( $10^{-7}$  M) of the chemoattractant resulted in a 15-fold increase in cellular viscosity and a 5.6-fold increase in shear modulus over nonstimulated cell values. In terms of the shear modulus, this result is consistent with the increases by factors of 3.4 for  $10^{-9}$  M and 7.3 for  $10^{-6}$  M found in the present study.

### Limitations of the model

Any model attempting to mimic the structural properties of the cell using a homogeneous, isotropic continuum description is open to criticism. Homogeneous representations fail to explicitly account for the detailed microstructure of the cell, and certainly neglect its capability for biological remodeling in response to a variety of factors. Despite their limitations, however, homogeneous, continuum descriptions have proved useful as a means of simulating cellular deformations under forcing, perhaps surprisingly so in view of the simplifications that they imply. To explain the underlying basis for a cell's mechanical properties, however, clearly requires a model that takes into account explicitly the microstructure and the biology.

Even within the constraints of a continuum model, however, there are further limitations in the development of a realistic model. Due to the absence of quantitative experimental data on the degree of hysteresis exhibited by neutrophils in indentation and the effects of fMLP on cortical tension, we needed to assume that the time constant of the cell's response in indentation ( $\mu_{\text{cell}}/G_{\text{cell}}$ ) remained constant and that the cortical tension was unaffected by the chemoattractant. These assumptions are in contrast to the observations that hysteresis actually increases with fMLP concentration (Worthen et al., 1989) and that fMLP induces F-actin formation beneath the plasma membrane (Saito et al., 2002), whereas cytochalasin-D disrupts F-actin formation and also decreases cortical tension in neutrophils by up to 60% (Ting-Beall et al., 1995). Although the results of the neutrophil indentation studies are somewhat limited by these considerations, the dimensionless transit-time expressions (Eqs. 21 and 22) are independent of any specific material properties (within the constraints of the expression given in Eq. 20). In the case that the dimensionless cortical tension exceeds the maximum limit explored in this study, however, it may be noted that, in the viscous-dominated limit ( $G \gg \Delta P$ ) the effect of solely increasing the cortical (surface) tension of the cell will generally be to increase the cell's transit time, because the effect of the tension is to

reduce the effective pressure driving the cell through the constriction. The degree of the effect, however, will depend upon the radius of curvature of the capillary examined (the effect is larger for smaller radii of curvature).

Several recent studies have focused on modeling the highly viscous, multi-lobed nucleus as a distinct entity within the neutrophil, with different mechanical properties from the less viscous cytoplasm (Tran-Son-Tay et al., 1998; Kan et al., 1998). This contrasts with the more traditional approach of treating the cell interior as a homogeneous medium that implicitly accounts for the effects of the cytoplasm and nucleus (in an averaged sense) using a single set of properties (Schmid-Schönbein et al., 1981; Dong et al., 1988; Evans and Yeung, 1989; Needham and Hochmuth, 1990). In this study, we chose to adopt the latter, homogeneous representation of the cell in the absence of sufficient experimental data on passive and fMLP-stimulated cells to allow for a unique determination of nuclear and cytoplasmic mechanical properties. We quantified the effects of fMLP on neutrophil mechanical properties by simulating indentation experiments (Table 1), in which deformations were relatively small in comparison with the deformations present in the capillary flow models (indentation depths were limited to 20% of the undeformed cellular diameter, whereas minimum capillary diameters were as small as 50% of the original cellular diameter). Again, despite this difference in the degree of deformations present in the models, the dimensionless expressions presented are valid within the constraints of a homogeneous cell model, because specific material property values do not enter the dimensionless transit time expressions (Eqs. 21 and 22). In interpreting the effects of fMLP on dimensional capillary transit times, however, we note that our estimates will likely represent a lower bound, because the model parameters were determined from indentation experiments that did not involve significant deformations of the nucleus (the nucleus is generally accepted to be more viscous than the cytoplasm (Tran-Son-Tay et al., 1998)).

## Neutrophil transit time

### *Dependence on capillary entrance geometry*

Rather than limit our study of capillary transit time to the specific values for the cellular properties found from indentation, we conducted a broad survey of the range of potential values. Despite the broad range of parameters explored, we were able to construct relatively simple algebraic relationships that can be used in subsequent studies involving neutrophil transit through pulmonary capillaries, such as the one previously conducted by our group (Huang et al., 2001). One of the primary findings of the present work is the strong dependence of transit time on entrance geometry as indicated by the influence of  $a^*$  in Eqs. 21 and 22.

The only other study that we are aware of in which neutrophil flow was modeled in a geometry other than a

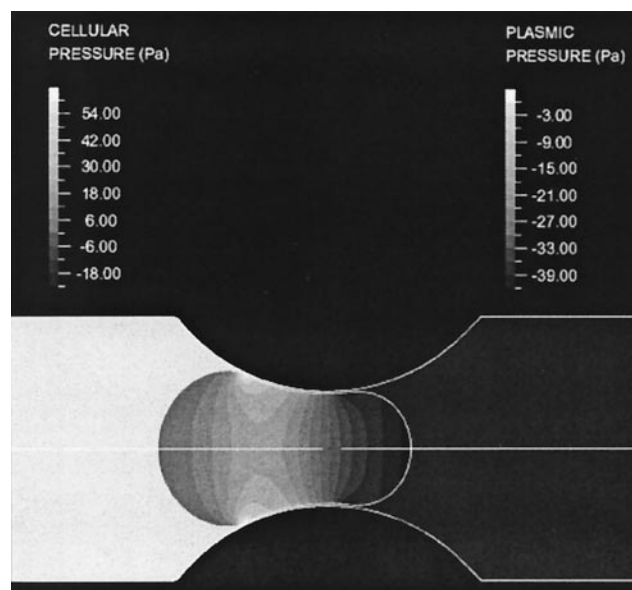


FIGURE 11 Pressure band plot illustrating the cellular pressure concentration near the capillary wall during cell entry into a capillary segment. A constant pressure drop of 40 Pa is applied across the ends of the capillary model (0 Pa at the upstream end and  $-40$  Pa at the downstream end).

blunt-ended micropipette is the study of Tran-Son-Tay et al. (1994) (see Finite element solution validation). In that study, it was found that neutrophil entry rate decreases with increasing taper angle, which is qualitatively consistent with the present results, though no direct comparison can be made between the two models due to differences in their geometries (constant constriction taper angle versus constant constriction radius of curvature).

Our results provide for a physical interpretation of the effect of entrance radius of curvature on transit time. In a balance of forces acting on the cell, the axial resultant force due to the driving pressure drop is opposed by the axial component of the resultant normal wall contact force (note that shear stress in the gap is negligible due to the large cell–plasma viscosity ratio, the slow rate of entry, and the constraint on minimum gap width, as shown in the Appendix). As the wall angle decreases, the magnitude of the wall contact force must increase to balance the resultant force from the driving pressure drop. Though the increase in contact force arises due to increases in both the contact area and the contact pressure, it is important to note that the contact pressure rises significantly (Fig. 11). The elevated contact pressure results in a radial pressure gradient from the area of contact to the center of the cell, and an axial pressure gradient from the center of the cell to the up- and downstream ends of the cell. The radial pressure gradient tends to squeeze the cell, whereas the axial pressure gradient tends to elongate it, in proportion to the magnitude of the contact pressure. The effect is considerable, as seen by the strong influence of  $a^*$  in the transit time results.

Interactions in the thin gap between the neutrophil and endothelium consequently play an important role in neutrophil entrance into and transit through a narrow capillary segment. Analysis of the detailed character of this interaction, however, is complicated by a number of factors. Previous simulations of micropipette aspiration (e.g., Drury and Dembo, 1999) have assumed that the interaction is frictionless and obtained results consistent with experiments, presumably because the viscosity ratio ( $\mu_{\text{cell}}/\mu_{\text{plasma}}$ ) is large. In vivo, however, the situation is complicated due to the presence of an endothelial glycocalyx that has been measured to be more than 1  $\mu\text{m}$  thick in capillaries of the hamster cremaster using intravital microscopy (Vink and Duling, 1996), and more than 0.1  $\mu\text{m}$  thick in arterioles and capillaries using electron microscopy (Rostgaard and Qvortrup, 1997). Recently, a number of studies have focused on simulating the effects of the glycocalyx on red blood cell flow in capillaries of uniform circular cross-section, modeling the endothelium lining layer as either an elastic solid (Damiano, 1998) or a compressible porous medium (Feng and Weinbaum, 2000), or using an osmotic model (Pries et al., 1997). Although significant progress has been made at better understanding and modeling the effects of the glycocalyx, there does not yet appear to be a consensus as to how to treat this glycoprotein-rich layer (Pries et al., 2000). Furthermore, the effects of the glycocalyx on reducing the functional capillary diameter appear to be more significant for flowing red blood cells than for leukocytes and stationary red blood cells, both of which invade the layer in vivo (Vink and Duling, 1996). In this study, we treated the glycocalyx as a rigid, 100-nm-thick layer that is highly permeable to plasma. We reasoned that, due to the presence of the glycocalyx, it was unlikely that the cell could approach much closer than this distance, and that the glycocalyx could serve as a lubricating layer, causing shear stresses in vivo to be even less important than in the micropipette experiments where they apparently are already insignificant. Moreover, as mentioned above, an assumption of this sort was required to prevent the cell from approaching unrealistically close ( $<10$  nm) to the endothelium. Incorporating a more sophisticated model for the glycocalyx presents a rich opportunity for further study but is beyond the scope of the present work.

#### Relative effects of capillary geometry and fMLP

Next we compare the relative effects of capillary geometry ( $R_{\text{min}}$  and  $a$ ) and fMLP-stimulation level on neutrophil transit time using the dimensionless transit time expression (Eq. 21) and the indentation results (Table 1) (relative effects on transit time should be physiologically meaningful despite the fact that the indentation experiments were carried out at room temperature). Assuming a trans-capillary pressure drop of 40 Pa, typical of neutrophil-blocked pulmonary capillary segments (Huang et al., 2001), an unde-

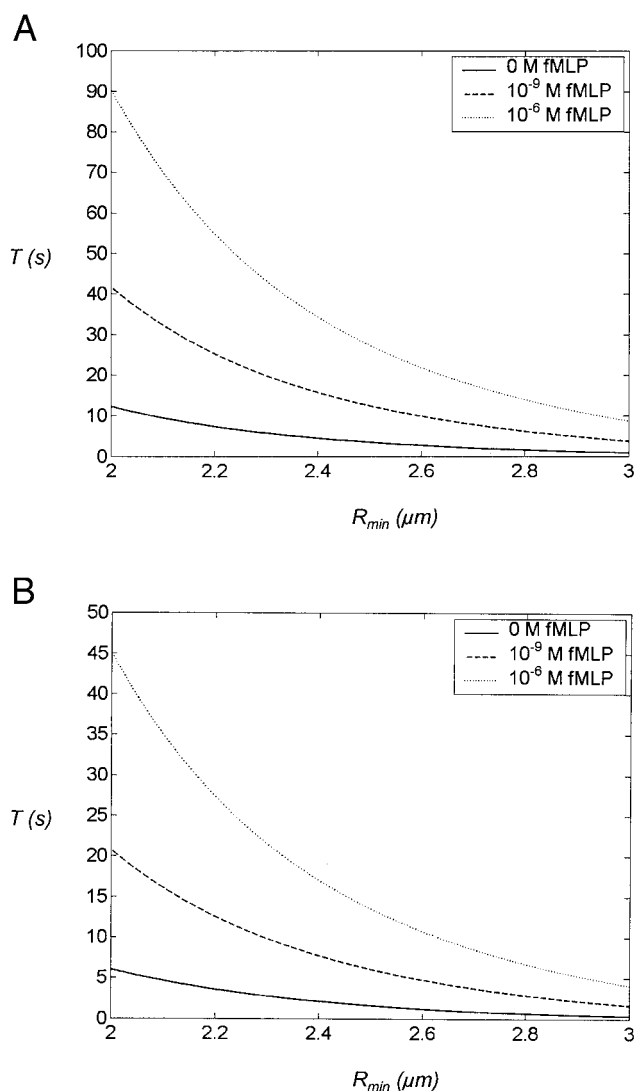


FIGURE 12 The dependence of neutrophil transit time ( $R_{\text{cell}} = 4 \mu\text{m}$ ) on minimum capillary constriction radius for three levels of fMLP concentration (0,  $10^{-9}$ , and  $10^{-6}$  M),  $\Delta P = 40$  Pa, and capillary constriction radii of curvature of (A) 5 and (B) 20  $\mu\text{m}$ .

formed cellular radius of 4  $\mu\text{m}$ , a cortical tension of 31 pN/ $\mu\text{m}$ , and constriction radii of curvature of 5 and 20  $\mu\text{m}$ , dimensional trans-capillary transit time versus minimum capillary constriction radius can be plotted for the three levels of fMLP concentration studied (Fig. 12 A, and B). Focusing on the narrowest capillary constriction analyzed,  $R_{\text{min}} = 2.0 \mu\text{m}$ , and the maximally stimulated cell,  $10^{-6}$  M fMLP, the effects of capillary entrance radius of curvature are seen to be significant: a four-fold increase in constriction radius of curvature (Fig. 12 A,  $a = 5$ ; Fig. 12 B,  $a = 20 \mu\text{m}$ ) results in a more than two-fold reduction in neutrophil transit time, from  $\sim 90$  to 45 s. The effects of fMLP on transit time are significant as well. Stimulation with  $10^{-9}$  and  $10^{-6}$  M concentrations of fMLP increase nonstimulated transit times by factors of  $\sim 3.4$  and 7.3, respectively, pri-

marily due to the increases in cellular viscosity induced by the chemoattractant. The dramatic effects of minimum capillary radius on transit time are evident in Fig. 12 A and B, where, for example, the maximally stimulated cell's transit time is increased three-fold from 9 to 27 s in going from  $R_{\min} = 3$  to  $2.5 \mu\text{m}$ , in the  $a = 5 \mu\text{m}$  case (Fig. 12 A).

Note that these calculations assume a pressure drop of 40 Pa, typical of an obstructed capillary segment, but that, depending on the geometry of the network, some fraction of segments would experience smaller values of  $\Delta P$  and consequently even longer transit times. Thus, the transit time of neutrophils through individual pulmonary capillaries is sensitive to fMLP-stimulation and capillary entrance geometry, network geometry, and minimum functional capillary radius.

As stated earlier, the effects of finite  $G^*$  on reducing neutrophil transit time can be significant, particularly for "mildly" constricted capillaries (e.g. Fig. 8 A,  $R^* = 0.75$  and Eq. 21). This finding is in agreement with the results of an in vivo study that compared transit times of neutrophils and rigid microspheres through rabbit lungs and found that 5–5.1- $\mu\text{m}$ -diameter rigid microspheres were delayed in their transit with respect to red blood cells in the same proportion (78% delayed) as deformable neutrophils with a mean diameter of  $6.4 \mu\text{m}$  (also 78% delayed) (Wiggs, et al., 1994). Furthermore, when the neutrophils were fixed with glutaraldehyde to prevent deformation, the proportion of delayed cells was in line with equivalently sized rigid microspheres (about 96%). These experimental results underscore the important role that neutrophil elasticity plays in vivo, allowing a  $6.4\text{-}\mu\text{m}$  cell to deform rapidly to a diameter of  $\sim 5 \mu\text{m}$  to transit mid-size capillaries, without a delay in transit with respect to erythrocytes. The results of the present study quantify the effects of fMLP on cellular elastic stiffness and viscosity, in addition to the implications of these changes on capillary transit time.

Despite the progress made in this study toward constructing a more realistic model of neutrophil flow through individual pulmonary capillaries, significant room for improvement remains. First, noncircular cross-sectional geometries (ellipsoidal and nonsymmetric geometries) are certain to influence cell transit times, and their effects must be represented in any realistic model of the pulmonary capillaries (Huang et al., 2001). Second, morphological studies are required to determine the physiological range of capillary entrance radius of curvature in the human lungs. Third, a more accurate model for the capillary endothelial glycocalyx is needed, and the effects of capillary wall compliance should be included. Although any changes in functional capillary diameter caused by a deforming neutrophil are probably of lesser importance, changes incurred during the normal respiratory cycle can be significant and should be accounted for in the neutrophil's transit time. Finally, the effects of biochemical and mechanical stimulation on neutrophil mechanical properties need to be better established. In particular, micropipette aspiration experiments on fMLP-

stimulated cells are needed to uniquely determine the changes in cortical tension associated with fMLP-stimulation, larger deformation experiments are required to account for the effects of the nucleus on the cell's stimulated response, and emerging micro-manipulative and imaging techniques are required to understand the origin of the observed macroscopic changes.

## APPENDIX

Using an order-of-magnitude analysis, the axial force driving the cell through the constriction,  $F_p$ , is that due to the imposed transcapillary pressure drop,  $\Delta P$ , and can be estimated to be  $F_p \sim \pi R_{\min}^2 \Delta P$ . Using the fact that the cell is (almost) incompressible, or cell volume is conserved during transit, we have that  $4/3 \pi R_{\text{cell}}^3 \approx \pi R_{\min}^2 l$ , where  $l$  is the approximate length of the elongated cell during transit. The retarding Couette flow-induced shear stress in the constriction gap is then  $\tau \sim \mu_{\text{plasma}} l / T \delta$ , which results in a retarding force of  $F_r \sim (\mu_{\text{plasma}} / T \delta) (2 \pi R_{\min} l)$ . For retarding shear stress-induced forces on the cell to be negligible compared to transcapillary pressure-drop-induced forces during transit, we must have that  $F_p \gg F_r$ . This force inequality can be rearranged as

$$T^* \gg \frac{\mu^*}{\delta^* R^{*5}}, \quad (\text{A1})$$

where  $\mu^* \equiv \mu_{\text{plasma}} / \mu_{\text{cell}}$ ,  $\delta^* \equiv \delta / R_{\text{cell}}$ ,  $R^* \equiv R_{\min} / R_{\text{cell}}$ , and  $T^* \equiv T \Delta P / \mu_{\text{cell}}$ . Substituting the fixed model parameter values,  $\mu_{\text{plasma}} = 0.001$  Pa·s,  $R_{\text{cell}} = 4 \mu\text{m}$ ,  $\delta = 0.1 \mu\text{m}$ , and choosing variable model parameters that maximize the right-hand side, namely,  $\mu_{\text{cell}} = 30.8$  Pa·s and  $R_{\min} = 2.5 \mu\text{m}$ , we obtain the maximum lower bound for  $T^*$ ,

$$T^* \gg 0.01. \quad (\text{A2})$$

Because typical dimensionless transit times in this study are of order 1 (Fig. 8, A, B, and C), the above criterion (A2) is satisfied. Thus the axial retarding force due to shear stress in the gap is insignificant compared to the axial driving force due to the effective transcapillary pressure drop. Moreover, even for gap sizes as small as 10 nm, the right-hand side would be increased to 0.1, so that the criterion would still be satisfied. Thus we find that cell transit time is independent of both plasma viscosity and gap size within the range of model parameters explored in this study, an assumption that has been made previously by other groups (Needham and Hochmuth, 1990; Tran-Son-Tay et al., 1994; Drury and Dembo, 1999) in analyzing neutrophil entrance into micropipettes and tapered tubes, and one that is consistent with the sharp cellular acceleration that we observed upon exit from the capillary constriction. The one obvious caveat to this conclusion is that it ignores any form of receptor–ligand interaction that could give rise to larger shear forces acting on the cell.

Funding contributions from the National Heart, Lung, and Blood Institute (HL33009 and HL64858) and the National Defense Science and Engineering Graduate fellowship awarded to M.B. are gratefully acknowledged.

## REFERENCES

- Bathe, K. J., H. Zhang, and M. H. Wang. 1995. Finite element analysis of incompressible and compressible fluid flows with free surfaces and structural interactions. *Comput. Struct.* 56:193–213.
- Bathe, K. J. 1996. *Finite Element Procedures*. Prentice Hall, N. J.
- Brezzi, F., and Fortin, M. 1991. *Mixed and Hybrid Finite Element Methods*. Springer-Verlag, New York.



- Damiano, E. R. 1998. The effect of the endothelial-cell glycocalyx on the motion of red blood cells through capillaries. *Microvasc. Res.* 55:77–91.
- Doerschuk, C. M. 2001. Mechanisms of leukocyte sequestration in inflamed lungs. *Microcirculation.* 8:71–88.
- Doerschuk, C. M., N. Beyers, H. O. Coxson, B. Wiggs, and J. C. Hogg. 1993. Comparison of neutrophil and capillary diameters and their relation to neutrophil sequestration in the lung. *J. Appl. Physiol.* 74:3040–3045.
- Dong, C., R. Skalak, K.-L. P. Sung, G. W. Schmid-Schönbein, and S. Chien. 1988. Passive deformation analysis of human leukocytes. *J. Biomech. Eng.* 110:27–36.
- Dong, C., R. Skalak, K.-L. P. Sung. 1991. Cytoplasmic rheology of passive neutrophils. *Biorheology.* 28:557–567.
- Dong, C., and R. Skalak. 1992. Leukocyte deformability: finite element modeling of large viscoelastic deformation. *J. Theor. Bio.* 158:173–193.
- Drury, J. L., and M. Dembo. 1999. Hydrodynamics of micropipette aspiration. *Biophys. J.* 76:110–128.
- Evans, E., and B. Kukan. 1984. Passive material behavior of granulocytes based on large deformation and recovery after deformation tests. *Blood.* 64:1028–1035.
- Evans, E., and A. Yeung. 1989. Apparent viscosity and cortical tension of blood granulocytes determined by micropipet aspiration. *Biophys. J.* 56:151–160.
- Feng, J., and S. Weinbaum. 2000. Lubrication theory in highly compressible porous media: the mechanics of skiing, from red cells to humans. *J. Fluid Mech.* 422:281–317.
- Fenton, B. M., D. W. Wilson, and G. R. Cokelet. 1985. Analysis of the effects of measured white blood cell entrance times on hemodynamics in a computer model of a microvascular bed. *Pflügers Arch.* 403:396–401.
- Frank, R. S., and M. A. Tsai. 1990. The behavior of human neutrophils during flow through capillary pores. *J. Biomech. Eng.* 112:227–282.
- Guntheroth, W. G., D. L. Luchtel, and I. Kawabori. 1982. Pulmonary microcirculation: tubules rather than sheet and post. *J. Appl. Physiol.* 53:510–515.
- Hochmuth, R. M., H. P. Ting-Beall, B. B. Beaty, D. Needham, and R. Tran-Son-Tay. 1993. Viscosity of passive human neutrophils undergoing small deformations. *Biophys. J.* 64: 1596–1601.
- Hogg, J. C., H. O. Coxson, M.-L. Brumwell, N. Beyers, C. M. Doerschuk, W. MacNee, and B. R. Wiggs. 1994. Erythrocyte and polymorphonuclear cell transit time and concentration in human pulmonary capillaries. *J. Appl. Physiol.* 77:1795–1800.
- Huang, Y., C. M. Doerschuk, and R. D. Kamm. 2001. Computational modeling of RBC and neutrophil transit through the pulmonary capillaries. *J. Appl. Physiol.* 90:545–564.
- Kan, H.-C., H. S. Udaykumar, W. Shyy, and R. Tran-Son-Tay. 1998. Hydrodynamics of a compound drop with application to leukocyte modeling. *Phys. Fluids* 10:760–774.
- Lien, D. C., W. W. Wagner, Jr., R. L. Capen, C. Haslett, W. L. Hanson, S. E. Hofmeister, P. M. Henson, and G. S. Worthen. 1987. Physiological neutrophil sequestration in the lung: visual evidence for localization in capillaries. *J. Appl. Physiol.* 62:1236–1243.
- Lien, D. C., G. S. Worthen, R. L. Capen, W. L. Hanson, L. L. Checkley, S. J. Janke, P. M. Henson, and W. W. Wagner, Jr. 1990. Neutrophil kinetics in the pulmonary microcirculation. Effects of pressure and flow in the dependent lung. *Am. Rev. Respir. Dis.* 141:953–959.
- Lien, D. C., P. M. Henson, R. L. Capen, J. E. Henson, W. L. Hanson, W. W. Wagner, Jr., and G. S. Worthen. 1991. Neutrophil kinetics in the pulmonary microcirculation during acute inflammation. *Lab. Invest.* 65:145–159.
- Lipowsky, H. H., D. Riedel, G. S. Shi. 1991. In vivo mechanical properties of leukocytes during adhesion to venular endothelium. *Biorheology.* 28:53–64.
- Motosugi, H., L. Graham, T. W. Noblitt, N. A. Doyle, W. M. Quinlan, Y. Li, and C. M. Doerschuk. 1996. Changes in neutrophil actin and shape during sequestration induced by complement fragments in rabbits. *Am. J. Pathol.* 149:963–973.
- Needham, D., and R. M. Hochmuth. 1990. Rapid flow of passive neutrophils into a 4  $\mu\text{m}$  pipet and measurement of cytoplasmic viscosity. *J. Biomech. Eng.* 112:269–276.
- Pries, A. R., T. W. Secomb, and P. Gaetgens. 2000. The endothelial surface layer. *Pflügers Arch. Eur. J. Physiol.* 440:653–666.
- Pries, A. R., T. W. Secomb, H. Jacobs, M. Sperandio, K. Osterloh, and P. Gaetgens. 1997. Microvascular blood flow resistance: role of endothelial surface layer. *Am. J. Physiol. Heart lin. Physiol.* 273:H2272–H2279.
- Rostgaard, J., and K. Qvortrup. 1997. Electron microscopic demonstrations of filamentous molecular sieve plugs in capillary fenestrae. *Microvasc. Res.* 53:1–13.
- Rugonyi, S., and K. J. Bathe. 2001. On finite element analysis of fluid flows fully coupled with structural interactions. *Comput. Model Eng. Sci.* 2:79–96.
- Saito, H., J. Lai, R. Rogers, and C. M. Doerschuk. 2002. Mechanical properties of rat bone marrow and circulating neutrophils and their responses to inflammatory mediators. *Blood.* 99:2207–2213.
- Schmid-Schönbein, G. W., K.-L. P. Sung, H. Tözere, R. Skalak, and S. Chien. 1981. Passive mechanical properties of human leukocytes. *Biophys. J.* 36:243–256.
- Skalak, R., C. Dong, and C. Zhu. 1990. Passive deformations and active motions of leukocytes. *J. Biomech. Eng.* 112:295–302.
- Sung, K. P., C. Dong, G. W. Schmid-Schönbein, S. Chien, and R. Skalak. 1988. Leukocyte relaxation properties. *Biophys. J.* 54:331–336.
- Sussman, T., and K. J. Bathe. 1987. A finite element formulation for nonlinear incompressible elastic and inelastic analysis. *Comput. Struct.* 26:357–409.
- Ting-Beall, H. P., A. S. Lee, and R. M. Hochmuth. 1995. Effect of cytochalasin D on the mechanical properties and morphology of passive human neutrophils. *Ann. Biomed. Eng.* 23:666–671.
- Tran-Son-Tay, R., D. Needham, A. Yeung, and R. M. Hochmuth. 1991. Time-dependent recovery of passive neutrophils after large deformation. *Biophys. J.* 60:856–866.
- Tran-Son-Tay, R., T. F. Kirk, III, D. V. Zhelev, and R. M. Hochmuth. 1994. Numerical simulation of the flow of highly viscous drops down a tapered tube. *J. Biomech. Eng.* 116:172–177.
- Tran-Son-Tay, R., H. C. Kan, H. S. Udaykumar, E. Damay, and W. Shyy. 1998. Rheological modeling of leukocytes. *Med. Biol. Eng. Comput.* 36:246–50.
- Tsai, M., R. S. Frank, and R. E. Waugh. 1993. Passive mechanical behavior of human neutrophils: power-law fluid. *Biophys. J.* 65:2078–2088.
- Vink, H., and B. R. Duling. 1996. Identification of distinct luminal domains for macromolecules, erythrocytes, and leukocytes within mammalian capillaries. *Circ. Res.* 79:581–589.
- Warnke, K. C. and T. C. Skalak. 1992. In vivo measurement of leukocyte viscosity during capillary plugging. *J. Biomech. Eng.* 114:533–538.
- Weibel, E. R. 1963. Morphometry of the Human Lung. New York: Academic.
- Wiggs, B. R., D. English, W. M. Quinlan, N. A. Doyle, J. C. Hogg, and C. M. Doerschuk. 1994. Contributions of capillary pathway size and neutrophil deformability to neutrophil transit through rabbit lungs. *J. Appl. Physiol.* 77:463–470.
- Worthen, G. S., B. Schwab, III, E. L. Elson, and G. P. Downey. 1989. Mechanics of stimulated neutrophils: cell stiffening induces retention in capillaries. *Science.* 245:183–186.
- Yeung, A., and E. Evans. 1989. Cortical shell-liquid core model for passive flow of liquid-like spherical cells into micropipets. *Biophys. J.* 56:139–149.
- Zahalak, G. I., W. B. McConnaughey, and E. L. Elson. 1990. Determination of cellular mechanical properties by cell poking, with an application to leukocytes. *J. Biomech. Eng.* 112:283–294.
- Zhelev, D. V., D. Needham, and R. M. Hochmuth. 1994. Role of the membrane cortex in neutrophil deformation in small pipets. *Biophys. J.* 67:696–705.